Highly efficient mid-infrared metasurface based on metallic rods and plate

Qian Sun (孙 倩)[2], Shuming Wang (王漱明)[1,3,*], Hui Liu (刘 辉)[1,3,], and Shining Zhu (祝世宁)[1,3]**

[1]*National Laboratory of Solid State Microstructures and School of Physics, Nanjing University, Nanjing 210093, China*
[2]*Beijing Institute of Space Mechanics and Electricity, Beijing 100076, China*
[3]*Collaborative Innovation Center of Advanced Microstructures, Nanjing 210093, China*
**Corresponding author: wangshuming@nju.edu.cn; **corresponding author: liuhui@nju.edu.cn*
Received November 27, 2015; accepted February 23, 2016; posted online April 6, 2016

Metasurface is a new kind of 2D metamaterial that is able to manage a variety of light beam modulations through steering the phase of the scattering waves. In this work, we utilize the metasurface to manipulate the light beam in the mid-infrared regime. By using the metallic rod and the plate structure, the metasurface presents a high polarization conversion efficiency and a wide working bandwidth. With specially rotated metallic rods, the metasurface can realize various light beam manipulations, such as negative reflection, beam collimation, and focusing. All of these results show that such a metasurface will have potential applications in future mid-infrared optics.

OCIS codes: 110.7348, 130.3060, 160.3918.
doi: 10.3788/COL201614.051101.

Mid-infrared optics has attracted more and more attention because the mid-infrared spectral region contains 'fingerprints' of the most common molecular vibrations. These provide information on a sample's molecular composition and coordination, which are crucial for materials analyses. Some greenhouse and pollution gases also have strong infrared signatures. In addition, imaging in the infrared is extremely important for thermal analysis, security, and materials inspection. However, the mid-infrared has been a challenging region for photonics; detectors made from narrow-bandgap materials are intrinsically noisy and efficient infrared-light emitters are difficult to be realized. The situation changed dramatically following the introduction of intersubband devices, such as quantum-well infrared photodetectors[1] and quantum cascade lasers[2,3]. Such an important range of light requires a variety of devices for precise light manipulation.

Metamaterials, a new kind of artificial material, represent a nontraditional approach to manipulating local and far-field light behavior, leading to exotic optical phenomena, such as negative refraction[4,5], super imaging[6–9], invisibility cloaking[10–18], magnetic plasmons[19–21], and optical black holes[22]. The building blocks of metamaterials are function-driven artificial meta-atoms, resulting in a great flexibility in tuning electromagnetic properties such as the effective electric permittivity and the effective magnetic permeability.

Recently, metasurfaces, a new class of metamaterials that consist of only a monolayer of planar metallic structures, have shown great promise for achieving full control of wavefronts of light with low fabrication cost, as they do not require complicated 3D nanofabrication techniques[23–25]. Metasurfaces are capable of generating abrupt interfacial phase changes and provide a unique way of controlling the local wavefront at the subwavelength scale[26–39]. A plethora of applications have already been proposed and demonstrated by using metasurfaces, such as wave plates for generating vortex beams[26,38], ultrathin metalenses[31,32], aberration-free quarter-wave plates (QWPs)[29], the spin Hall effect of light[36,39,40], polarization-dependent unidirectional surface plasmon-polariton (SPP) excitation[37–39], spin-controlled photonics[39], achromatic lenses[41], and invisible cloaking[42]. In addition, a mid-infrared metasurface also has advances in simple fabrication, which only need matured lithography.

Various designs of diffractive elements of metasurfaces, such as the H-shape, V-shape, and metallic rod, have been reported. H-shape has worked well in the microwave regime in spatial light-SPP conversion and light beam manipulation[33]. With specially designed parameters of the H-shape structure, the effective permittivity and permeability of the metasurface can be tuned at will by exciting the electric and magnetic resonances in it. The V-shape structure is the most famous building block of the metasurface, and has been used in the first so-called "metasurface" work[26]. By choosing different sizes and angles of the V-shape, the scattering wave from the V-shape structures with the opposite polarization to the incident wave carries a special additional phase. With only four carefully designed 'Vs', the desired phase array can be obtained. The negative refraction and orbital momentum light generation have been consequently realized with this metasurface in the visible and near-infrared regimes. In this work, we employ another promising diffractive element of metasurfaces, the metallic rod and plate, to obtain the high efficiency and wide bandwidth metasurface.

It is well known that the metallic rod can support an electric resonance in a certain frequency along the rod. According to the dipole momentum theory in Ref. [43], when the incident light is circularly polarized, we can

obtain an additional phase from the scattering light, refractive light, and reflective light, with the opposite circular polarization. The additional phase is just twice the rotating angle of the metallic rod against the x–y coordinate. This result can also be understood in the language of Berry phase and the Rashba effect in optics[44]. Therefore, by only rotating every metallic rod in a large 2D array to the special designed angles, one can easily obtain the desired phase array that can manipulate the incident light beam. However, such a metasurface design has a defect in the light conversion efficiency into the working polarized light, due to the low cross section of merely the metallic rod. To solve this problem, a metallic plate was added, as well as a dielectric spacer, under the rods to introduce a high reflection of scattering light[45]. Thus, an effective Fabry–Perot (F–P) cavity composed of the upper metallic rod array and the lower metallic plate has been obtained, which leads to a high conversion efficiency. It has been reported to be 80% in the near-infrared regime[45], above 90% at telecom wavelengths[46,47], and almost unity at longer wavelengths in this work. Such structure also has an advantage in the wide working bandwidth, since the electric resonance of the metallic rod is also quite wide. Considering the simplicity of fabrication, the metasurface based on a metallic rod and plate is a quite promising choice.

The geometry of the single metallic rod and plate is plotted in Fig. 1(a). In our work, the geometric parameters of the rod are the length $l = 3400$ nm, the width $w = 1200$ nm, and the height $h = 200$ nm. Considering the fabrication defect, the corners of the metallic bar are modified into a circular profile, with a radius $r = 300$ nm. Such a metallic rod can support the electric resonance in the mid-infrared regime, with the center wavelength at

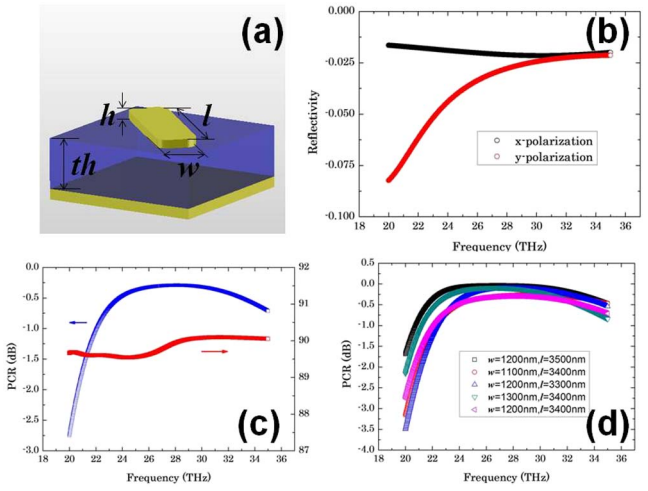

Fig. 1. (a) Geometric scheme of a single metallic rod and plate, (b) the reflectivity with x- or y-polarized incidence, (c) the PCR and phase difference between the x and y component of the reflecting wave when incident on a single 45° rotated metallic rod and plate structure, and (d) the PCRs with different parameters of the rod.

10.6 μm (28.3 THz), corresponding to the typical output wavelength of the CO_2 laser. The material of the rod is gold, with the permittivity obeying the Drude model $\varepsilon = \varepsilon_\infty - \omega_p^2/(\omega^2 + i\gamma\omega)$, where $\varepsilon_\infty = 1$, $\omega_p = 1.37 \times 10^{16}$ rad/s, and $\gamma = 1.95 \times 10^{12}$ rad/s. The middle dielectric layer is chosen to be a BaF_2 layer, which is transparent in the mid-infrared regime with the refractive index equal to 1.43. The thickness of this layer is th = 1200 nm, leading to an optimal F–P cavity that presents the largest reflection and polarization conversion. The bottom layer is a reflective gold plate.

The numerical simulation was carried out by CST Microwave Studio. Such a single metallic rod and plate has a nearly unity reflection, with both linear polarizations along the long and short axis of the rod, as presented in Fig. 1(b). We take the 45° rotated rod case as an example to present the working capability of the single metallic rod and plate structure. The 45° rotated rod and plate structure can work as a half-wave plate. The polarization along the x/y axis changes to the opposite polarization[46,47]. The incident light is an x-polarized linear wave, the reflective wave converts to a y-polarized wave with high efficiency, thus leading to the 90° ($\pi/4$) additional phase added to the reflective wave. This means that the metallic rod and plate system works quite well. The resulted polarization conversion ratio (PCR) is shown in Fig. 1(c). It can be observed that the PCR is very high in a wide range of the frequency, from about 22 to 34 THz. This is a quite wide frequency range that has promising applications. In addition, the rod structure is also defect tolerant, as shown in Fig. 1(d). The PCR changes a little with the parameters that will be introduced by fabrication, etc. The width and length of the rod has changed by 200 nm, with the PCR remaining at a quite high level.

Using this highly efficient diffractive element, we can manipulate the reflecting wave by introducing an additional wave vector. For example, if the rotating angles of the rods along the x axis obey the expression

$$\phi = \xi \times x \times k_0, \tag{1}$$

the additional wave vector of the reflecting wave along the x axis will be $2 \times \xi \times k_0$, introduced by the metasurface. Therefore, for normal incidence, the reflecting wave reflects along the angle $\theta = \arctan(2\xi)$. It should be mentioned that when $2\xi > 1$, the wave vector of the reflecting wave will be larger than k_0, which means that the reflecting wave is not the propagating wave but the evanescent wave, namely, the surface wave. This leads to the conversion from the spatial wave to the surface wave. In Fig. 2, we present the case for $\xi = 0.25$, with $\phi = 0.25 \times x \times k_0$ and $k_0 = 2\pi/\lambda$, where $\lambda = 10.6$ μm ($f = 28.3$ THz). The geometric scheme is presented in Fig. 2(a), with the period of the rod array being 4 μm. The electric field distribution at 10.6 μm is plotted in Fig. 2(c), and the additional reflecting angle is 26.6°. Such additional wave vectors can also be introduced at different wavelengths. In Figs. 2(b)

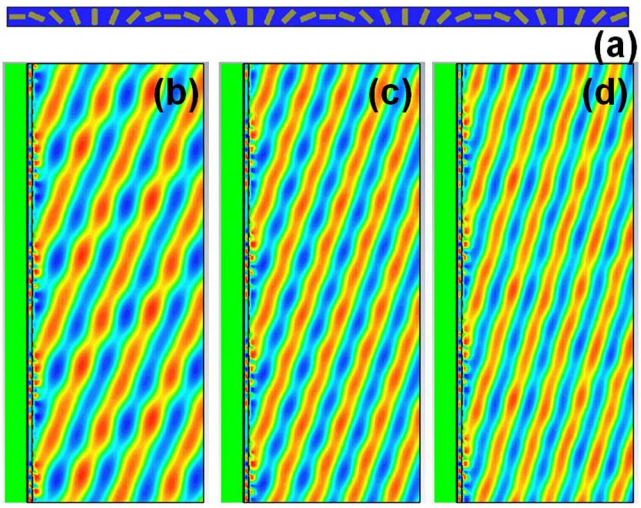

Fig. 2. (a) Geometric scheme of the reflection manipulation; the reflections with different frequencies, (b) 24, (c) 28.3, (d) and 32 THz.

and 2(d), the reflecting waves also have additional reflecting angles, while the reflecting angles are different for different wavelengths.

Negative reflection can also be obtained when the incident angle is smaller than the additional reflecting angle introduced by the metasurface, 26.6°. Here, we choose the incident angle to be 5.7°. An obvious negative reflection is observed with the incident wave and reflecting wave at the same side of the normal line, in Fig. 3.

Focusing can be considered as the most important function of the planar metasurface. In order to focus an incident circularly polarized wave, a flat lensing surface must undergo a spatially varying phase shift. To achieve a phase profile equivalent to a conventional cylindrical lens, the following expression governs the relationship between the rotation angle ϕ and the location of rods x:

$$\varphi = -0.5k_0\left(\sqrt{f^2 + x^2} - f\right), \tag{2}$$

where f is the focal length of the lens. The geometric scheme of the metasurface lens is shown in Fig. 4(a).

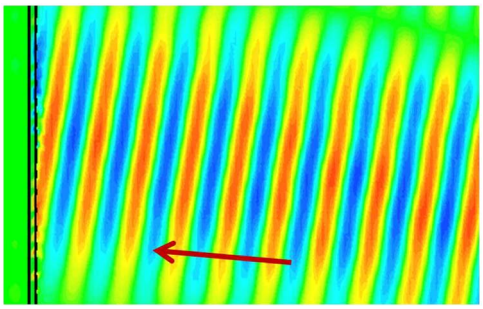

Fig. 3. Negative reflection with the incident angle being 5.7° at 28.3 THz. The incident wave is marked by the red arrow.

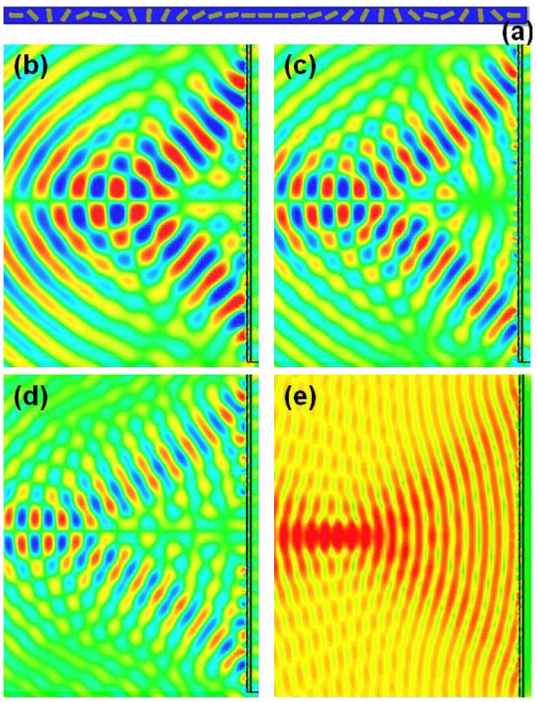

Fig. 4. (a) Geometric scheme; the focusing with different frequencies (b) 24, (c) 28.3, and (d) 32 THz. (e) The amplitude of E_x at 28.3 THz.

The metasurface lens is composed of 32 diffractive elements with the rotating angles of rods obeying Eq. (2) and the period being 4 μm. The focusing electric fields along the z axis, the propagating direction, with different wavelengths 24, 28.3, and 32 THz are plotted in Figs. 4(b), 4(c), and 4(d), respectively. The metasurface can well focus the reflecting wave at the focal length of $f = 50$ μm with the wavelength of 10.6 μm (28.3 THz). For a better observation of the focusing effect, the amplitude of electric field along the x axis, along the metasurface, is presented in Fig. 3(e). The focusing wavefront is well formed. The focusing effects at different wavelengths have different focal lengths for dispersion. For dispersion, the focal length increases with larger frequency, but they still have good focusing performance.

Finally, we introduce the cosine-Gauss beam by using the metasurface axicon lens. Such a metasurface is made

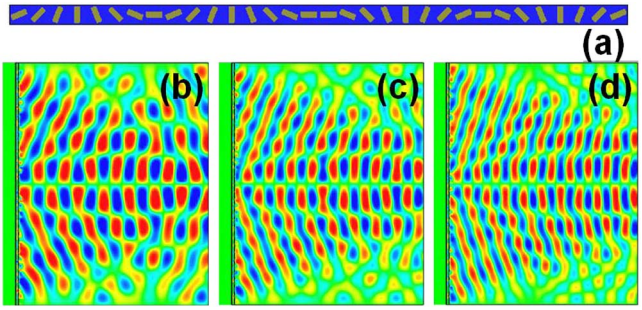

Fig. 5. (a) Geometric scheme; collimations with different frequencies (b) 24, (c) 28.3, and (d) 32 THz.

from two oppositely linear-tuned phase arrays. Without loss the generality, we use two metasurfaces with the rotating angles of the rods obeying Eq. (1) but opposite sign of ξ to realize the cosine-Gauss beam. The numerical simulation results are shown in Fig. 5. The good cosine-Gauss beams are observed in Figs. 5(b), 5(c), and 5(d), at 24, 28.3, and 32 THz, respectively. The wide bandwidth of the working mechanism is also found. For the dispersion, the focal length enlarges with increasing frequency.

In conclusion, we utilize a metasurface to manipulate a light beam in the mid-infrared regime. By using the metallic rod and plate structure, the metasurface can present a high polarization conversion efficiency and a wide working bandwidth. With different rotating angles of the metallic rods, the metasurface can realize negative reflection, beam collimation, and beam focusing. All of these results show that such a metasurface will have potential applications in future mid-infrared optics.

This work was supported by the National "973" Program of China (No. 2012CB933501) and the Program of "The Invention of the China Academy of Space Technology".

References

1. B. F. Levine, J. Appl. Phys. **74**, R1 (1993).
2. J. Faist, F. Capasso, D. L. Sivco, C. Sirtori, A. L. Hutchinson, and A. Y. Cho, Science **264**, 553 (1994).
3. S. Kumar, Chin. Opt. Lett. **9**, 110003 (2011).
4. R. A. Shelby, D. R. Smith, and S. Schultz, Science **292**, 77 (2001).
5. J. Valentine, S. Zhang, T. Zentgraf, E. Ulin-Avila, D. A. Genov, G. Bartal, and X. Zhang, Nature **455**, 376 (2008).
6. J. B. Pendry, Phys. Rev. Lett. **85**, 3966 (2000).
7. N. Fang, H. Lee, C. Sun, and X. Zhang, Science **308**, 534 (2005).
8. T. Taubner, D. Korobkin, Y. Urzhumov, G. Shvets, and R. Hillenbrand, Science **313**, 1595 (2006).
9. Z. Liu, H. Lee, Y. Xiong, C. Sun, and X. Zhang, Science **315**, 1686 (2007).
10. J. B. Pendry, D. Schurig, and D. R. Smith, Science **312**, 1780 (2006).
11. U. Leonhardt, Science **312**, 1777 (2006).
12. D. Schurig, J. J. Mock, B. J. Justice, S. A. Cummer, J. B. Pendry, A. F. Starr, and D. R. Smith, Science **314**, 977 (2006).
13. V. M. Shalaev, Nat. Photon. **1**, 41 (2007).
14. J. Valentine, J. Li, T. Zentgraf, G. Bartal, and X. Zhang, Nat. Mater. **8**, 568 (2009).
15. L. H. Gabrielli, J. Cardenas, C. B. Poitras, and M. Lipson, Nat. Photon. **3**, 461 (2009).
16. T. Ergin, N. Stenger, P. Brenner, J. B. Pendry, and M. Wegener, Science **328**, 337 (2010).
17. B. Edwards, A. Alu, M. G. Silveirinha, and N. Engheta, Phys. Rev. Lett. **103**, 153901 (2009).
18. X. Liu, L. Zhang, J. Zhou, J. Shi, Z. Wang, and D. Liu, Chin. Opt. Lett. **12**, 121601 (2014).
19. H. Liu, D. A. Genov, D. M. Wu, Y. M. Liu, Z. W. Liu, C. Sun, S. N. Zhu, and X. Zhang, Phys. Rev. B **76**, 073101 (2007).
20. H. Liu, D. A. Genov, D. M. Wu, Y. M. Liu, J. M. Steele, C. Sun, S. N. Zhu, and X. Zhang, Phys. Rev. Lett. **97**, 243902 (2006).
21. S. M. Wang, T. Li, H. Liu, F. M. Wang, S. N. Zhu, and X. Zhang, Opt. Express **16**, 3560 (2008).
22. C. Sheng, H. Liu, Y. Wang, S. N. Zhu, and D. Genov, Nat. Photon. **7**, 902 (2013).
23. S. Jeon, E. Menard, J. U. Park, J. Maria, M. Meitl, J. Zaumseil, and J. A. Rogers, Adv. Mater. **16**, 1369 (2004).
24. M. S. Rill, C. Plet, M. Thiel, I. Staude, G. Von Freymann, S. Linden, and M. Wegener, Nat. Mater. **7**, 543 (2008).
25. N. Liu, H. Liu, S. N. Zhu, and H. Giessen, Nat. Photon. **3**, 157 (2009).
26. N. Yu, P. Genevet, M. A. Kats, F. Aieta, J. P. Tetienne, F. Capasso, and Z. Gaburro, Science **334**, 333 (2012).
27. X. Ni, N. K. Emani, A. V. Kildishev, A. Boltasseva, and V. M. Shalaev, Science **335**, 427 (2012).
28. L. Huang, X. Z. Chen, H. Muhlenbernd, G. X. Li, B. F. Bai, Q. F. Tan, G. F. Jin, T. Zentgraf, and S. Zhang, Nano Lett. **12**, 5750 (2012).
29. M. Kang, T. Feng, H. T. Wang, and J. Li, Opt. Express **20**, 15882 (2012).
30. N. Yu, F. Aieta, P. Genevet, M. A. Kats, Z. Gaburro, and F. Capasso, Nano Lett. **12**, 6328 (2012).
31. F. Aieta, P. Genevet, M. A. Kats, N. F. Yu, R. Blanchard, Z. Gahurro, and F. Capasso, Nano Lett. **12**, 4932 (2012).
32. X. Chen, L. L. Huang, H. Muhlenbernd, G. X. Li, B. F. Bai, Q. F. Tan, G. F. Jin, C. W. Qiu, S. Zhang, and T. Zentgraf, Nat. Commun. **3**, 1198 (2012).
33. S. Sun, Q. He, S. Y. Xiao, Q. Xu, X. Li, and L. Zhou, Nat. Mater. **11**, 426 (2012).
34. S. Sun, K. Y. Yang, C. M. Wang, T. K. Juan, W. T. Chen, C. Y. Liao, Q. He, S. Y. Xiao, W. T. Kung, G. Y. Guo, L. Zhou, and D. P. Tsai, Nano Lett. **12**, 6223 (2012).
35. X. Ni, S. Ishii, A. V. Kildishev, and V. M. Shalaev, Light Sci. Appl. **2**, e72 (2013).
36. X. Yin, Z. Ye, J. Rho, Y. Wang, and X. Zhang, Science **339**, 1405 (2013).
37. L. Huang, X. Z. Chen, B. F. Bai, Q. F. Tan, G. F. Jin, T. Zentgraf, and S. Zhang, Light Sci. Appl. **2**, e70 (2013).
38. J. Lin, J. P. B. Mueller, Q. Wang, H. Yuan, N. Antoniou, X. C. Yuan, and F. Capasso, Science **340**, 331 (2013).
39. N. Shitrit, I. Yulevich, E. Maguid, D. Ozeri, D. Veksler, V. Kleiner, and E. Hasman, Science **340**, 724 (2013).
40. S. Xiao, F. Zhong, H. Liu, S. Zhu, and J. Li, Nat. Commun. **6**, 8360 (2015).
41. F. Aieta, M. A. Kats, P. Genevet, and F. Capasso, Science **347**, 1342 (2015).
42. X. Ni, Z. J. Wong, M. Mrejen, Y. Wang, and X. Zhang, Science **349**, 1310 (2015).
43. X. Chen, L. Huang, H. Muhlenbernd, G. Li, B. Bai, Q. Tan, G. Jin, C. Qiu, S. Zhang, and T. Zentgraf, Nat. Commun. **3**, 1198 (2012).
44. Nir Shitrit, Shai Maayani, Dekel Veksler, V. Kleiner, and E. Hasman, Opt. Lett. **38**, 4358 (2013).
45. G. Zheng, Nat. Nanotechnol. **10**, 308 (2015).
46. Y. Yang, Nano Lett. **14**, 1394 (2014).
47. F. Ding, Z. Wang, S. He, V. M. Shalaev, and A. V. Kildishev, ACS Nano. **9**, 4111 (2015).